When nature meets technology: AI-informed discovery of soil-water-root physical interaction

Anthony Kwan Leung[1*]*, Jianbin* Liu[1], and *Zhenliang* Jiang[1]

[1]Department of Civil and Environmental Engineering, the Hong Kong University of Science and Technology, Hong Kong SAR

Abstract. Nature-based solution using vegetation has been considered as a sustainable and environmentally friendly approach to improve slope performance through root reinforcement and variations of soil matric suction upon transpiration. During plant growth, roots explore soil pore space. How fundamentally the pore structure might evolve with time following root growth dynamics and how this dynamic soil–root interaction may modify the hydraulic properties of unsaturated soils remain unclear. This paper reports the use of advanced technologies including artificial intelligence (AI) to aid the discovery of soil–root–water physical interaction and the characterisation of the hydraulic properties of rooted soils. A newly developed miniature unsaturated triaxial apparatus that enables rooted soil samples to subject to simultaneous *in-situ* loading and X-ray imaging is introduced. An AI-informed image processing technique is illustrated, aiming to enhance the reliability of phase segmentation of X-ray computer tomography (CT) images of four-phase unsaturated rooted soils for quantifying 3-D pore structure and root phenotype. New discoveries of how roots interact with the pore space, including the dynamic changes in the distribution, orientation and connectivity of soil pore sizes, and how this pore-level information can be used to explain the hydraulic properties are discussed.

1 Introduction

Rainfall-induced slope failure has been one of the major natural hazards in tropical and subtropical regions, including Hong Kong and some parts of the Greater Bay Area of China, where precipitation is becoming more extreme due to global warming. Nature-based solution using vegetation is a sustainable and environmentally friendly means to improve the stability of shallow slopes [1]. Integrating vegetation into the built environment brings multiple environmental and societal benefits: (i) offsetting carbon use; (ii) creating pathways for carbon sequestration; (iii) offering ecological improvements to plant biodiversity and recovery of ecosystem functions; and (iv) providing an aesthetically pleasing appearance of transport earthworks in the built environment. These benefits will improve the quality of life of individuals in the community, directly contributing to the vision of carbon neutrality set by governments worldwide.

Plants affect the stability of shallow soils through root reinforcement [2, 3]; as soil slides, roots that cut across the slide plane provide anchorage to stabilise the soils by mobilising the soil–root interfacial properties and root tensile or/and bending strength [4] until they are broken (breakage failure) or pulled out from the soil (pull-out failure). Investigation on mechanical soil–root interaction have been extensively conducted since 1970s and are still a topic of major interest nowadays. Recent advancements include the uses of classic elastoplastic framework [5, 6] and fabric anisotropy [7, 8] to interpret and understand the hydromechanical responses of saturated and unsaturated rooted soils observed in the laboratory when subject to different stress paths (triaxial compression and triaxial extension [3]; direct tension [9]). Advanced numerical modelling means [4, 10] have also been developed to capture the soil–root load transfer mechanisms at their interface for more accurate modelling of vegetation-related problems such as the stability of slopes [11] and trees [4].

In addition to mechanical reinforcement, plants can affect soil stability by varying the soil water content through root-water uptake upon plant transpiration. The transpiration-induced reduction in soil water content, hence the increase in soil matric suction (referred to as hydrological reinforcement) could increase soil shear strength [12]. The increase in soil strength due to plant transpiration is found to be significantly correlated with the ratio of root to shoot biomass [13, 14]. Indeed, some field monitoring [2, 15] and centrifuge modelling works [16, 17] have shown that slopes covered with vegetation preserved higher suction than bare slopes, contributing to increases in the slope's factor of safety and delay of slope failure [16]. In some case studies [18], however, not much suction was preserved due to the formation of preferential flow paths and increased rainfall infiltration as the roots that penetrate to depths decomposed [19], or/and soil shrinks upon drying by root water uptake [18], especially for the case of fine-grained soils of which the volume change is sensitive to soil moisture variation.

As plant roots explore the soil pore space to search for nutrients and resources to support their growth, the soil pore structure, such as size, orientation and connectivity, can be altered (Fig. 1). Given the fact that the hydraulic properties of unsaturated soils including

---

* Corresponding author: ceanthony@ust.hk

water retention curve (WRC) and hydraulic conductivity function (HCF) primarily depend on the pore structure, it can be hypothesised that the presence of plant roots modify these soil properties. Scalan and Hinz [20] used a conceptual model on the basis of the capillarity law to illustrate the root effects on WRC; for a given soil water content, a root present in a pore throat makes the pore diameter smaller and thus the capillary height higher, returning a higher matric suction than the bare soil. Experiments aiming to examine the hypothesis were extremely rare, with only a few exceptions (Rahardjo et al. [15]; Jotisankasa and Sirirattanachat [21]). More fundamental and systematic studies are urgently needed to quantify how plant roots, and their growth dynamics, interact with soil and how this soil–root physical interaction affects these soil hydraulic properties. Indeed, correctly characterising root-induced changes in soil hydraulic properties is vital to carrying out seepage analysis and predicting the distribution of pore-water pressure in vegetated soil slopes, in addition to considering the effects of plant transpiration.
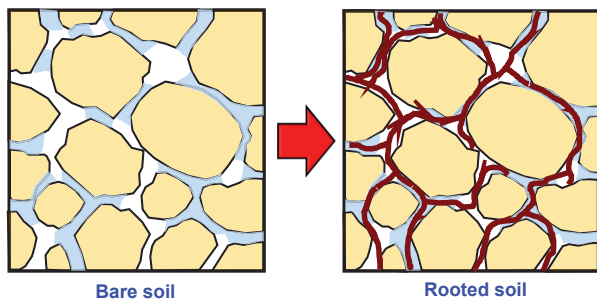

Bare soil   **Rooted soil**

Fig. 1. A conceptual model showing root permeation in soil pore space and potential influence on soil pore structure

This paper first presents some experimental evidence of how the presence of plant roots affect the hydraulic properties of unsaturated soils (WRC and HCF) based on the observations made from pot experiments. Then, two new experimental tools were introduced, namely (1) X-ray aided suction-controlled mini-triaxial system; and (2) AI-informed phase segmentation algorithm. These tools aim to aid the new discovery of pore-level soil–root–water physical interaction. Detailed discussion on how the segmentation of multi-phase unsaturated rooted soil sample (grain, root, air and water) can be performed with reduced uncertainty will be given. The pore-level information obtained from the processed X-ray images, such as 3-D soil pore structures and root phenotype, will then be used to explain the root-induced changes in the hydraulic properties observed at the element-level.

2 Root-induced changes in hydraulic properties of unsaturated soils

This section provides theoretical consideration based on some hypothesis of soil–root physical interaction. Some experimental evidence collected from existing data and those obtained from recent laboratory testing campaigns are provided to illustrate how roots modify the hydraulic properties of soils (WRC and HCF).

2.1 Theoretical consideration

Based on the consideration in Fig. 1, it is reasonable to hypothesise that plant roots explore, and hence modify, the soil pore space by occupying a certain void volume. The framework herein considers mainly the fine roots of which the diameter is comparable to that of soil pore. Coarse structural roots that have much larger diameters are deemed not to affect the soil pore-size distribution. Accordingly, a phase diagram of an unsaturated rooted soil, which is constituted by four phases, namely solid, water, air and root, can be constructed (Fig. 2; [22, 23]). Increase in root volume due to plant growth is quantified by root volume ratio (R_v; ratio of total root volume to soil volume), which is used to quantify any void volume reduction. To account for the effects of root decay upon mortality or turnover of fine roots, an additional term, root decay ratio (η, defined as the volumetric percentage of root decayed), is introduced [23] in the phase diagram. This term governs the volume of void 'returned' to the soil due to the loss of root biomass upon decomposition. Although roots shrink as they lose moisture, Boldrin et al. [24] showed that roots start to exhibit a significant reduction in diameter when root suction exceeds 1 MPa. Given the range of interest in this study (< 100 kPa), any root volume change upon wet–dry cycles is deemed negligible. As a result, based on the phase diagram, the following void ratio function that accounts for the root effects can be expressed as:

$$e = \frac{e_0 - (1-\eta)R_v(1+e_0)}{1 + (1-\eta)R_v(1+e_0)} \quad (1)$$

where e_0 is the initial void ratio of fallow soil (without vegetation). Note that (1) R_v varies from zero (i.e. bare soil) to an upper bound of $e_0/(1+e_0)$ when all void volume is occupied by the roots; and (2) η varies from zero to a certain value less than 1.0. The exact upper bound of η is plant species dependent, referring to the residual amount of volumetric root content at a steady-state of decomposition. The void ratio function can be input to any void ratio-dependent WRC model, such as those proposed by Gallipoli et al. [25]; hence, the WRC model for unsaturated rooted soil can be expressed as:

$$S_r = \left[1 + \left(\frac{se^{m_4}}{m_3 \exp\left(-k \dfrac{e_r}{e_{r0}}\right)} \right)^{m_2} \right]^{-m_1} \quad (2)$$

where S_r is the soil degree of saturation; s is the matric suction; and m_1 [-], m_2 [-], m_3 [kPa], m_4 [-] are the model parameters. m_1 and m_2 control the shape of a WRC, while m_3 and m_4 are related to the air-entry value (AEV) of the bare soil; k is a model parameter that controls the rate of reduction of the AEV due to root decay and this parameter is dependent on the plant type and soil type; e_r is the macro void ratio "returned" from root decay:

$$e_r = \frac{\eta R_v(1+e_0)}{1 + (1-\eta)R_v(1+e_0)} \quad (3)$$

and e_{r0} is the void ratio occupied by roots (i.e. $e_0 - e$), when η is zero. Hence, by knowing the WRC of the bare soil, R_v, η and k, WRC of an unsaturated rooted soil may be predicted.
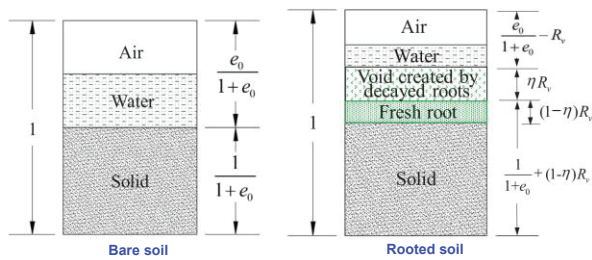

Fig. 2. Phase diagram of a three-phase unsaturated soil (left) and a four-phase unsaturated rooted soil (right) considering both root growth and decomposition [23]

2.2 Observations from pot and column tests

2.2.1 Water retention curves

Figure 3 compares the main drying WRCs of compacted silty sand (with a dry density of 1777 kg/m^3, 98% of the maximum dry density) with and without planting with a shrub, *Scheffera heptaphylla*, reported by Ng et al. [22] and Ni et al. [23]. All the WRCs were obtained by relating the volumetric water content (VWC) and matric suction respectively measured by a moisture probe and a tensiometer (with an AEV of 100 kPa) installed in a circular planter (600 mm diameter and 450 mm height). Two plant spacings (60 and 180 mm, denoted as S60 and S180) were considered when measuring the WRCs.
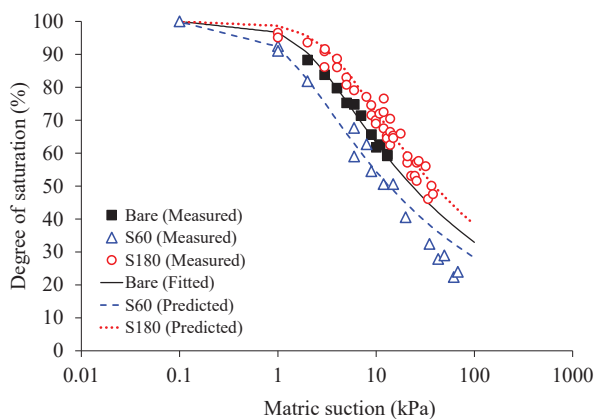

Fig. 3. Measured and predicted WRCs of compacted silty sand with and without vegetation [23]

The test results showed that for the case of wide plant spacing (i.e. 180 mm), the presence of roots improved the water retention ability by increasing the AEV when compared with the bare soil. The desorption rate (i.e. the amount of VWC reduction for a given suction increase), however, was similar. When the plant spacing was close (i.e. 60 mm), the AEV of the rooted soil was reduced. Post-test root excavation and inspection suggested prominent root decay in the case of S60, attributable to intense shrub-shrub competition for the resources in the soil. Further measurements showed that the value of R_v

and η for the S60 case was 0.044±0.004 and 11.0±1.2%, respectively, whilst those for the S180 case was 0.034 ± 0.005 and 1.0±1.0%, respectively. By using Eqs (1) to (3), the WRCs of the rooted soils can be estimated and the computed WRCs are superimposed in Fig. 3. The corresponding parameters are summarised in Table 1. The computed results matched well with the test data. Based on this, it is postulated that the improvement of the water retention behaviour for the 180 mm spacing case was attributed to the pore clogging by roots as they grew and permeated in the soil pore space, causing an apparent densification of the soil. On the contrary, the reduced water retention behaviour for the case of 60 mm spacing was associated with root decay, a process during which the root biomass reduced, 'returning' the volume of void originally occupied by the roots and causing an apparent loosening of the soil [23].

Table 1. Summary of the input parameters for the WRCs of bare and rooted soils.

Test	Parameters						
	m_1	m_2	m_3 (kPa)	m_4	e_0	R_v (mm^3 mm^{-3})	η (%)
S60	0.15	1.9	0.18	3.51	0.5	0.044	11
S180	0.15	1.9	0.18	3.51	0.5	0.034	1.0

Rahardjo et al. [15] also reported a comparison of the WRCs of intact alluvium planted with two grass species, namely orange jasmine (*Myrrata exotica*) and vetiver grass (*Chrysopgon zizanioides*), measured by a Tempe cell. Their results depicted substantial improvement of the soil water retention capability by roots, though the degree of improvement in terms of AEV and desorption rate appeared to depend on the grass species. Jotisankasa and Sirirattanachat [21] used a similar test method as Ni et al. [23] to measure the WRCs of silt and clayey sand planted with *C. zizanioides* for a range of root length density (RLD; ratio of the total root length to the soil volume). This study, however, observed a reduction in the water retention of both soil types; it was postulated to be due to the formation of micro-cracks in the soil upon repeated wet–dry cycles during the measurements.

2.2.2 Unsaturated hydraulic conductivity functions

Test data of HCF of unsaturated rooted soils is much rare. As far as the authors are aware, only three studies, Song et al. [26], Jotisankasa and Sirirattanachat [21] and Ni et al. [27], have conducted systematic experiments to characterise the root effects on HCF. All of these studies adopted the instantaneous profile method [IPM; 28, 29] to determine the soil hydraulic conductivity as suction varied with time and space. Taking Ni et al. [27] as an example, the experimental setup was a cylindrical pot (200 mm in diameter and 400 mm in height) filled with compacted soil (silty sand) that was planted with a grass (*Cynodon dactylon*) or a shrub (*S. heptaphylla*) species. Four pairs of soil moisture probes and tensiometers were

installed along pot depth to monitor the spatiotemporal variations of VWC and matric suction, respectively, when the vegetated soils were subjected to controlled top boundary conditions such as evapotranspiration and rainfall. By setting the datum at the pot base, the suction measured can be converted to hydraulic head. Hence, the hydraulic gradient at any depth and any elapsed time ($\nabla H_{m,t_{ave}}$) can be determined by:

$$\nabla H_{m,t_{ave}} = \frac{\nabla \psi}{\nabla z} = \frac{1}{2}\left(\frac{\psi_{u,i-1}-\psi_{l,i-1}}{\Delta z} + \frac{\psi_{u,i}-\psi_{l,i}}{\Delta z}\right) - 1 \quad (4)$$

where $\psi_{u,i}$ and $\psi_{u,i-1}$ are the values of matric suction measured by the upper tensiometer at time t_i and t_{i-1}, respectively; $\psi_{l,i}$ and $\psi_{l,i-1}$ are the values of matric suction measured by the lower tensiometer at time t_i and t_{i-1}, respectively; and Δz is the distance between any two tensiometers. By determining the area bounded by two VWC-depth profiles with two consecutive elapsed time ($\Delta V_{t_{ave}}$), the water flow rate at any depth and any elapsed time ($q_{m,t_{ave}}$) can be determined by:

$$q_{m,t_{ave}} = \frac{q_{0,t_{ave}}}{2} = \frac{\Delta V_{t_{ave}}}{2 \cdot A \cdot \Delta t_{ave}} \quad (5)$$

where Δt_{ave} is taken as $(t_i - t_{i-1})$; and A is the cross-sectional area of the specimen. Finally, according to the Darcy's law, unsaturated hydraulic conductivity of the soil at the middle of the two tensiometers at the average elapsed time of evaporation, t_{ave} ($t_{ave} = (t_{i-1} + t_i)/2$), can be calculated as follows:

$$k_{m,t_{ave}} = \frac{q_{m,t_{ave}}}{\nabla H_{m,t_{ave}}} \quad (6)$$

Figure 4 shows the measured results of the HCFs of bare soil, grass-vegetated soil, tree-vegetated soil and soils vegetated with both species (i.e. mixed). The measured hydraulic conductivity $k_{m,tave}$ was normalised by the saturated value (k_s) of the respective case separately measured. Based on the WRC models (Eq. (2)), the HCFs can be predicted by the equation proposed by van Genuchten [30], as follows:

$$k_r = S_r^{0.5}[1-(1-S_r^{\frac{1}{m}})^m]^2 \quad (7)$$

where k_r is the relative hydraulic conductivity when $k_{m,tave}$ is normalised by k_s. The results show that the reduction rates of k_r with respect to an increase in suction in the two cases vegetated with one single species were lower than that of the bare case. In contrast, the reduction rate for the mixed-vegetated case was higher. This means that the presence of roots does not only affect the AEV, but also plays a significant role in affecting the water flow. The prediction made by Eq. (7) showed good match for the bare soil case, but not the three vegetated cases. The predicted reduction rates of k_r were different from the measured ones. The observed discrepancies are somewhat expected because the van Genuchten (1980)'s equation, and indeed most of the other existing HCF equations, do not consider the root effects on the changes in the soil pore size distribution (Fig. 1), and hence the hydraulic properties.

Jotisankasa and Sirirattanachat [21] also adopted the IPM to measure the effects of roots of *C. zizanioides* on HCF of compacted silt and clayey sand. The vegetated soils displayed greater $k_{m,tave}$ in suctions below 10 kPa (i.e. near the AEV). Depending on the root contents (measured by RLD in this case), the HCF of the clayey sand exhibited dual-permeability behaviour; as suction was lower than 1 kPa, the $k_{m,tave}$ was up to two orders of magnitude higher than that of the bare soil. Song et al. [26] measured the HCF of a clay vegetated with *C. dactylon* and *C. zizanioides* grown in the field. Based on the IPM, the HCFs of intact block samples of vegetated soils were determined. Their results showed that the HCFs were significantly affected by desiccation cracks developed upon evapotranspiration. The values of $k_{m,tave}$ of the cracked bare soil were almost two orders of magnitude higher than that of the crack-free compacted soils prepared in the laboratory. The roots of *C. dactylon* appeared to restrict the development of cracks in the soils and hence the $k_{m,tave}$ increased by almost one order of magnitude. The roots of *C. zizanioides*, however, made an increase in $k_{m,tave}$ to be almost two orders of magnitude larger than the crack-free compacted soil.
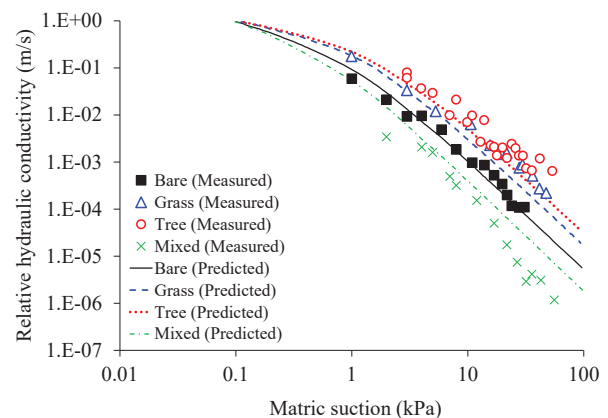

Fig. 4. Measured normlised HCFs of compacted silty sand vegetated with a grass or a tree species [27]

3 X-ray-aided suction-controlled mini-triaxial system

Evidently, measurements made from the pot and column tests have shown that roots can significantly modify the soil hydraulic properties, primarily attributable to the physical soil–root interaction as roots explore the soil pore space. This interaction is transient and varies with the root growth dynamics. Fundamental understanding of the underlying mechanisms by which plant roots take to modify the soil hydraulic properties requires detailed pore-level studies. However, there exist technological challenges that limit the advances of detailed pore-level investigation of soil–water–root physical interaction.

X-ray computed tomography (CT) has been used to visualise and hence quantify pore structure and grain kinematics of soil samples under controlled loading conditions. Existing apparatus design allow simultaneous *in-situ* loading and X-ray imaging of unsaturated soil samples are available [31, 32, 33], but there exist some common limitations: (1) unable to provide independent

and continuous control of hydromechanical stress path in the net normal stress–deviatoric stress–matric suction space; (2) unable to control matric suction or only able to control a limited range (< 7 kPa); and (3) unable to optimise the size of the apparatus (hence sample size) whilst maintaining the quality of X-ray images taken.

This section introduces a new suction-controlled miniature triaxial apparatus that can be placed in an X-ray μCT scanner for testing the micro-hydromechanical (mHM) behaviour of unsaturated soils [34]. The system allows the *in-situ* 3-D visualisation and quantification of the evolution of soil microstructure upon different controlled HM triaxial stress paths. The apparatus can control a wide range of matric suctions through two suction-controlled methods (hanging column and axis translation techniques), whilst permitting independent control of net normal stress.

3.1 Design of apparatus

Figure 5 shows the miniature suction-controlled triaxial apparatus, which is a self-compact system that can be placed in an X-ray μCT scanner. The apparatus integrates a loading unit, an integrated cell pressure and suction control unit, and a sample installation unit.
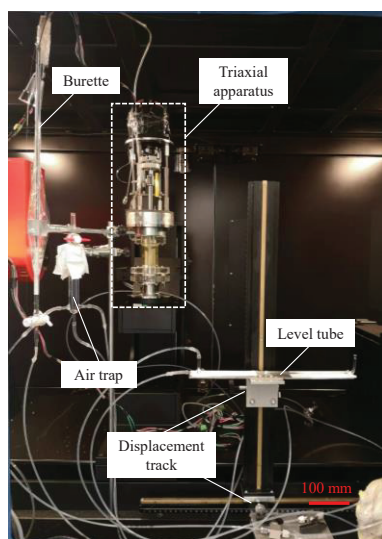

Fig. 5. Overview of a newly developed miniature suction-controlled triaxial apparatus in an X-ray μCT scanner [34]

The loading unit comprises a strain-controlled linear actuator to apply an axial load, a load cell to monitor the axial load, a linear variable differential transformer (LVDT) to monitor the axial displacement, a loading rod for axial force transmission, a rigid chamber to retain confining pressure and a base pedestal embedded with a high AEV ceramic disk (500 kPa). To ensure X-ray transparency, the chamber of the triaxial cell is made of polymethyl methacrylate (PMMA). The middle part of the sample stage is also made of PMMA to enable visual inspection of any diffused air bubble in the reservoir used for water supply to the sample.

During operation, each X-ray scan could take up to 3 h under a maintained strain condition to obtain quality images. To correct for any time effect on the system performance, an axial strain was applied to a dummy

PMMA sample (Young's modulus of 3 GPa) to reach an initial deviatoric stress of 261.8 kPa and the strain was maintained for 3 h. The findings reveal that the deviatoric stress reduced with time exponentially, and a drop of deviatoric stress of 7.6% was observed after 3 h. The drop of deviatoric stress was associated with the stress relaxation of the system (plastic compression of O-rings and backlash of the actuator). Thus, the time-dependent stress relaxation and any friction generated between the loading rod and radial seal during a complete test is corrected, from this point onward.

An integrated cell pressure and suction control unit was designed to enable the flexible control of a wide range of matric suction from 0 to 500 kPa and a smooth transition between the use of the hanging column and axis translation techniques (ASTM: D 6836-02 2003). Negative pore-water pressure, u_w, of the soil samples, hence, matric suction (i.e. 0–10 kPa, by assuming pore-air pressure, u_a, to be atmospheric), can be controlled using the hanging column method by adjusting the height of the level tube reference to the elevation of the ceramic disk. When applying a higher suction using the axis translation technique, the level tube should first be returned to the same level as the ceramic disk (i.e. $u_w = 0$). Then, air pressure, hence, matric suction, of up to 500 kPa, can be controlled by a regulator.

A sample installation unit (Fig. 6) was designed to minimise the (1) disturbance of small-sized samples that have low bearing capacity and the (2) eccentric moment induced when tubing the sample cap to the sample stage that often happens in conventional triaxial apparatus. Prior to sample installation, the chamber and the loading rod were fixed at desired positions, and the sample together with the mould was moved to the baseplate. In the case of preparing loose sample, a small vacuum can be applied through the loading rod to provide temporary sample stability. Subsequently, the mould was removed, and the whole assembly was detached from the clamps and bolted to the rolling stage of an X-ray CT scanner for testing. The whole system was connected to a laptop for computerised loading control and data acquisition.
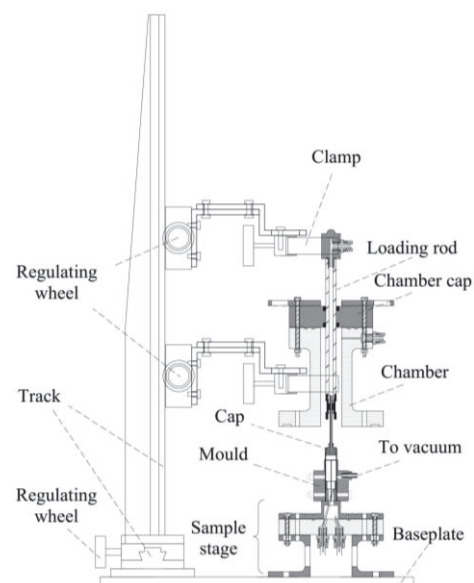

Fig. 6. A schematic diagram showing the detailed design of the tailor-made sample installation unit [34]

3.2 Capabilities of measuring WRCs

A series of experiments were carried out to demonstrate the capability of the developed apparatus to measure the WRCs of bare soil under controlled stress states.

3.2.1 Materials and methods

Toyoura sand (Toyoura Keiseki Kogyo Co., Ltd.), which is composed of quartz (92.6%), aluminium oxide (3.7%) and iron (III) oxide (0.7%), was used for testing. The sand is poorly graded, with a particle size ranged from 0.102 to 0.339 mm and a particle size of 50% passing (d_{50}) of 0.242 mm. This particle size distribution makes this sand ideal for CT imaging and visualising the grain kinematics and transport of pore fluid, given the limited resolution of the X-ray CT scanner (9.87 μm). Three samples (10 mm diameter and 20 mm height) were prepared by the dry deposition method and they were installed in the apparatus (Fig. 5) using the tailor-design unit depicted in Fig. 6. The target relative density of the sand samples was 51.6% (categorised as medium dense), corresponding to the initial void ratio of 0.76.

After installation, the three samples were saturated by capillarity through the application of a water head of 100 mm above the head of the samples. At equilibrium, these samples were then sent to X-ray scan using the X-ray scanner available at the Hong Kong University of Science and Technology (model: Nanovoxel 3000, Sanying precision instrument co. Ltd.). The voltage, current and resolution of the scanner were set to be 105 kV, 200 µA and 9.87 µm, respectively. After scanning, these samples were isotropically loaded to different net mean stresses ($p - u_a$, p is the total mean stress and u_a is the pore-air pressure which is atmospheric), namely 0, 100 and 200 kPa, and were then X-ray scanned again under the maintained stress condition. Subsequently, the three samples were dried by increasing the matric suction ($u_a - u_w$, where u_w is the pore-water pressure) from 0 to 8 kPa in steps using the hanging column method. At each equilibrium step of suction, any volume of water expelled from the samples was recorded to determine the degree of saturation.

The X-ray images obtained were reconstructed using the software, Voxel Studio Recon. Phase segmentation of the reconstructed images was subsequently conducted using the Otsu method [35]. For each sand sample, three images representing three different phases (i.e. solid, water and air) were exported for further image analyses. To measure the effect of net mean stress on the evolution of pore structure, the pore network model (PNM; [36]) of each sample was constructed. In the PNM, each of the individual pores scanned is represented by a ball with an equivalent volume, whereas each pore throat is represented by a cylindrical stick. The stick has a radius corresponding to the equivalent throat area, whereas the length corresponds to the geometrical centre between two connected balls. Figure 7 shows an example of the 3-D images of the three phases (solid, water and air) of the samples subject to a net mean stress of 100 kPa and a matric suction of 3 kPa, after phase segmentation.
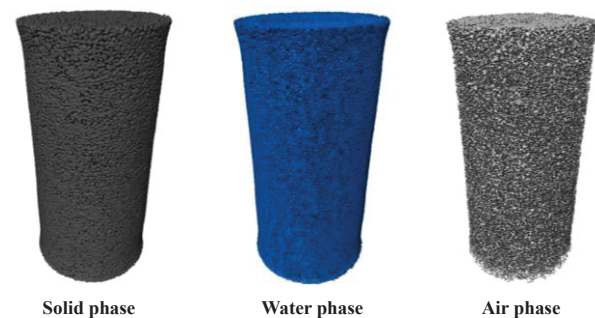

Solid phase   **Water phase**   **Air phase**

Fig. 7. A 3-D view of the solid, water and air phase of the sand sample subject to a net mean stress of 100 kPa and a matric suction of 3 kPa, after phase segmentation from a CT image.

3.2.2 Observations and discussion

Figure 8 compares the WRCs of the three sand samples measured under different maintained stress conditions. The initial degree of saturation of all the samples were not 100% because of the ink-bottle effect when capillary rise was used as a means of sample saturation. After applying the net mean stresses of 100 and 200 kPa, the void ratio of the samples decreased from 0.76 to 0.43 and 0.38, respectively. The difference in the void ratio partially explained the initial difference in the degree of saturation. Evidently, the application of net mean stress increased the water retention capability of the sand, as displayed by the reducing rate of desorption; at a given suction, the VWC retained in the sand subject to a higher net mean stress was larger.
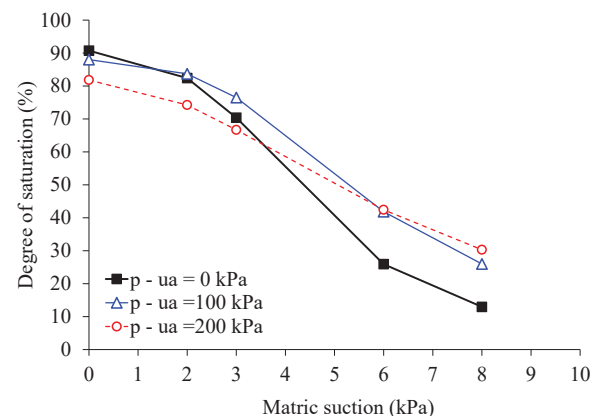

Fig. 8. WRCs of sand samples subjected to three different net mean stresses of 0, 100 and 200 kPa.

In general, the observations are consistent with those reported by previous studies [37, 38], which explored the effects of net mean stress on the WRC of sandy soil. It has been hypothesised that the net mean stress affects not only the void ratio but also the pore structure, but this hypothesis has not been tested previously. Based on the image analysis using the PNM, the pore structure of the three sand samples, including the size, orientation, connectivity and tortuosity, can be obtained to examine the hypothesis. Figure 9 shows the frequency diagrams of the equivalent pore diameter of the three samples. Evidently, applying net mean stress to the sand samples caused a simultaneous downward and leftward shift of the distribution, suggesting an overall reduction of the number and volume of pore sizes. The amount of shift

of the pore size distribution appears to be similar due to the compressibility of the sand. As expected, the pore size distribution of the non-plastic sand did not display any major change after experiencing the drying cycle, regardless of the net mean stress considered.
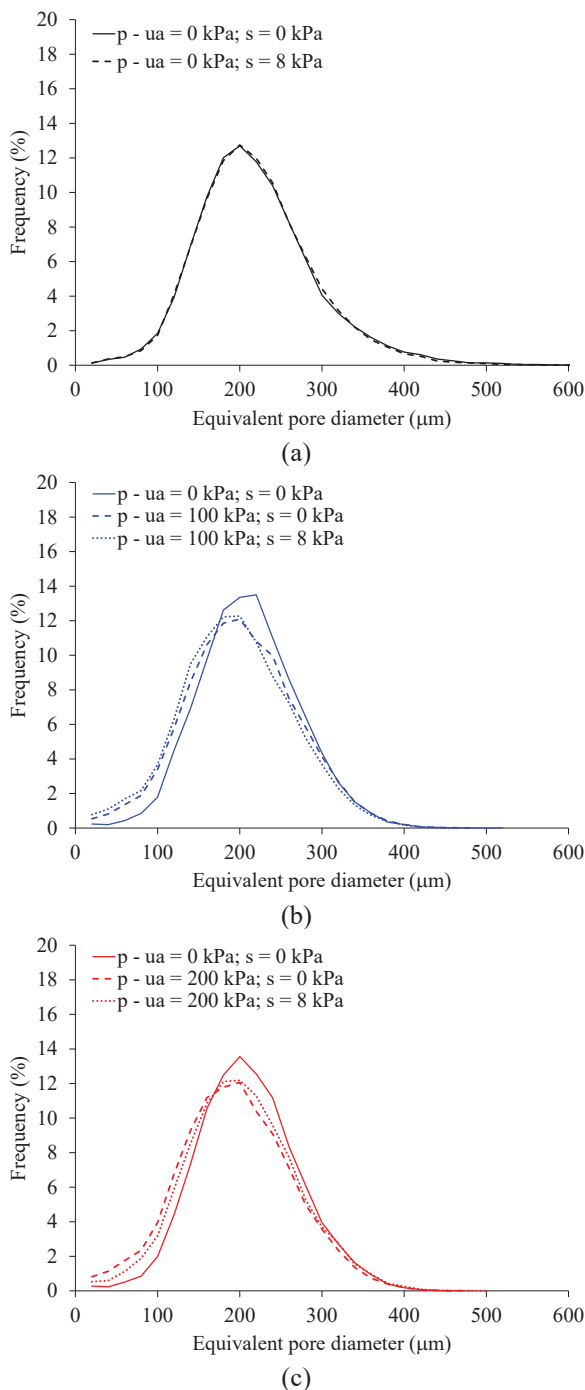

(a)

(b)

(c)

Fig. 9. Frequency diagrams of the equivalent pore diameter of the samples subjected to different net mean stresses; (a) 0 kPa; (b) 100 kPa and (c) 200 kPa, all obtained before and after drying (at suctions of zero and 8 kPa).

Figure 10 depicts the frequency diagrams of the pore throat orientation of the three sand samples. The angle presented in the x-axis of the figure is referenced to the upward vertical direction (i.e. defined as 0º). The angle 90º refers to the horizontal direction of pore throats. Most of the pores of all three samples orientated towards the horizontal direction preferentially, probably because

of the anisotropy introduced by the sample preparation method by dry deposition. Evidently, applying net mean stress to up to 200 kPa introduced no practical change in the pore orientation. Further image analysis showed that the volume of isolated pores (which can be a measure of pore connectivity) for the sand samples under zero net mean stress was only 0.09% of the total pore volume. The high pore connectivity may be somewhat expected as the sand tested was poorly or narrowly graded with a limited range of particle size. Similarly, applying the net mean stress to up to 200 kPa did not display any appreciable change in the volume of isolated pores.

The pore-level image analysis aided by the PNM suggested that it is predominantly the pore size and its distribution that changed the WRC of the poorly-graded sand for the range of net mean stresses examined. Other pore structural parameters including connectivity and orientation remained practically unchanged. Further investigation is needed in the future to examine if the same mechanisms of pore structure evolution apply to other types of sand of different angularities and wider gradings tested under a wider range of net mean stress.
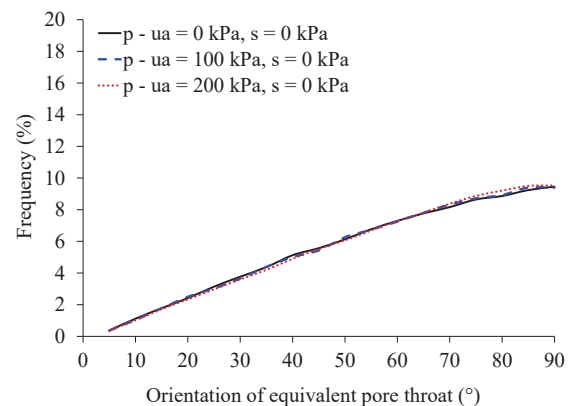

Fig. 10. Frequency diagrams of the pore throat orientation of the samples subjected to the three different net mean stresses, all obtained at suction = 0 kPa.

4 Artificial Intelligence-informed phase segmentation algorithm

After taking the CT images of an unsaturated rooted soil sample, the next important step is to conduct accurate and reliable image segmentation for the different phases existed in the sample, in this case, soil grains/particles, roots, air and water. Correct phase segmentation of a CT image is vital as the information obtained is the basis for subsequent image-based analysis (herein referred to as CT-IBA). Of particular interest in soil bioengineering application is the analysis of the volumetric fraction of different phases, pore structure and root phenotype, which all underpin the subsequent estimation of the soil hydraulic properties including k_s.

There exist various means and algorithms to conduct accurate and efficient phase segmentation, yet carrying out reliable or repeatable segmentation remains a major challenge due to the lack of effective means to reliably separate the boundary among the different phases of an unsaturated rooted soil sample. Given the coefficient of X-ray attenuation of some phases, such as water, roots,

and organic matters, are close [39], phase segmentation could be affected by the partial volume effects caused by the 3-D blurring and image sampling [40].

Learning-based methods, such as machine learning, deep learning and transfer learning, have been used to perform phase segmentation of CT images [41, 42, 43]. Machine learning approach uses predefined features of an CT image to feed the learning process, whereas deep learning case addresses features as part of the embedded learning process [44]. However, these learning-based methods contain uncertainties, such as operator bias, susceptibility to partial volume effect and image quality, and multi-process involved when analysing images of multiphase objects like rooted soils [45]. Indeed, most of the existing segmentation methods are deterministic, without considering any uncertainty involved during the phase segmentation of the CT images of rooted soils.

This section introduces new methods and procedures that (1) quantify segmentation uncertainty (SU) when using machine learning-based phase segmentation of CT images of rooted soils; and (2) analyse the propagation of SU from one step of CT-IBA to the next ones. Based on these new methods, effects of SU and the propagation of the uncertainty on the estimation of the hydraulic properties of rooted soils are discussed.

4.1 Phase segmentation methods

Figure 11 shows the methods of quantifying SU and its propagation. Firstly, a 3-D X-ray CT image (Fig. 11(a)) is pre-processed to reduce intraphase noise and enhance interphase edges. A non-local mean (NLM) algorithm can be used to smooth the phase interior of the images [46]. The edges in the image can be further enhanced by unsharp masking [47] to subtract a blurred copy of the image from the original one and to rescale the copied image to obtain the same contrast of large (i.e. low-frequency) structures as in an input image. The values of blur radius and mask weight can be varied to adjust the edge enhancement, so that the edges of the copied image can be enhanced without severely distorting the boundaries among phases.
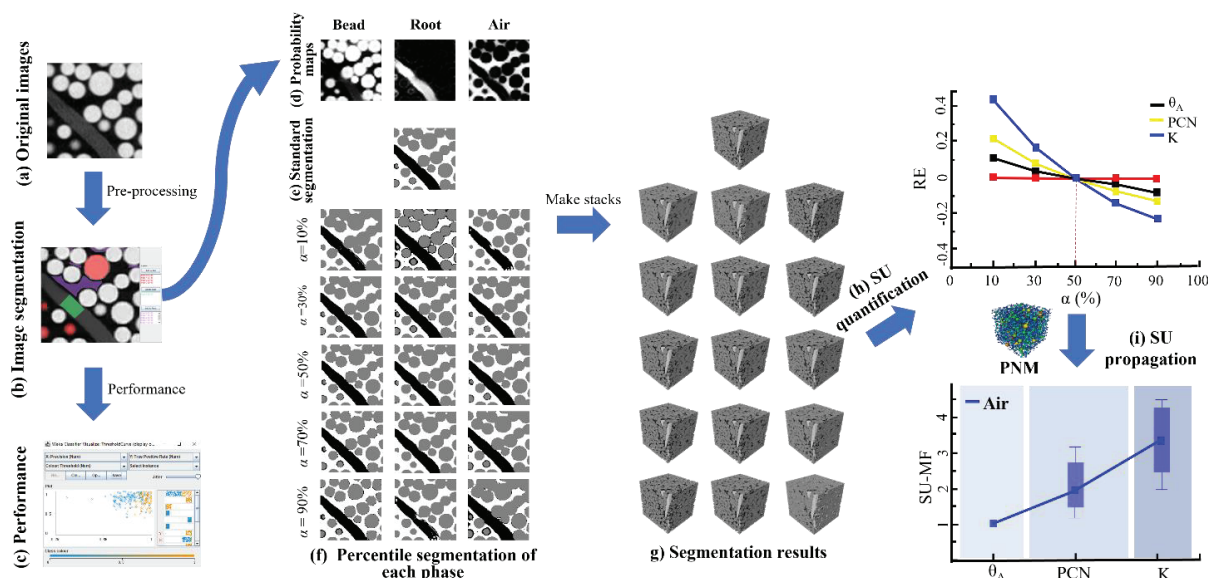
Secondly, phase segmentation of the CT image (Fig. 11(b)) is conducted by a supervised machine learning method, aiming to generate segmentation probability maps (PMs). Weka Trainable Segmentation, which is an open-source plugin in Fiji software [48], can be used to perform image segmentation due to its unique function in generating a PM for each phase, providing a basis for the subsequent percentile segmentation. The training datasets and features of each phase of an unsaturated rooted soil sample (grain, root, air and water) can be manually selected as inputs for segmentation for the random forest algorithm. Then, the model training is performed to return PMs, of which the performance can be evaluated against some indicators ([49]; Fig. 11(c)). The satisfactory PMs (Fig. 11(d)) can then be used for subsequent CT-IBA.

Based on the PMs, percentile segmentation (PS, [50]; Fig. 11(f)) can be carried out. This method assigns each phase of a rooted soil sample (grain, root, air and water) to a pixel (x, y) with the maximum probability among different channels (Ch = grain, root, air and water). Subsequently, the algorithm compares the probability, $P(x, y, Ch)$, of each voxel of the CT image with a given segmentation percentile (α); if the $P(x, y, Ch)$ is larger or equal to α, then the voxel is assigned to the phase of interest, else it is assigned to other phase that has the largest probability. This process repeats until all voxels in the image are assigned a phase. The value of α is fundamentally subjective and can be set at any desired percentile for the phase of concern in an image. For example, in Fig. 11(f), there are five values of α (10%, 30%, 50%, 70% and 90%) for a three-phase dry rooted soil sample (grain, root and air or pore); there are thus 15 combinations of calculation, the output of which is expressed in mean and standard deviation ($\mu \pm \sigma$) for subsequent SU quantification analysis.

Based on the outcomes of the segmentation by the image stacking (Fig. 11(g)), volumetric fraction analysis can be conducted to estimate the volumetric contents of each phase. This information was used for subsequent analysis of pore structure and root phenotype. The root relevant phenotypic properties are root equivalent
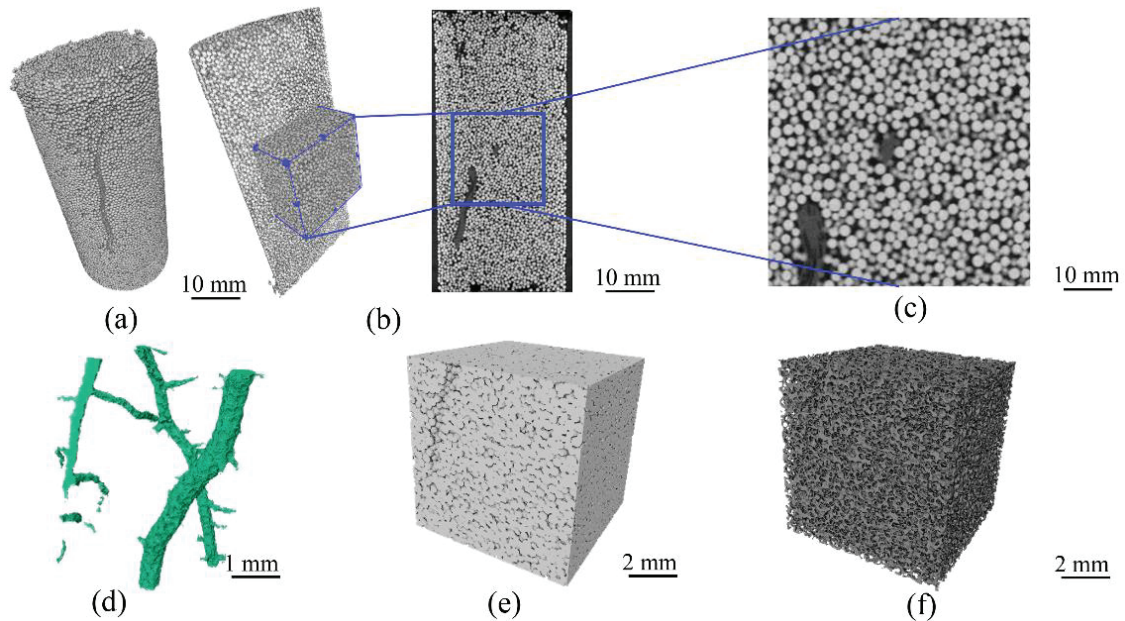

Fig. 11. Steps of quantifying segmentation uncertainty and its propagation

Fig. 12. Reconstructed CT images of dry rooted bead: (a) a 3-D CT image after phase segmentation; (b) a 2-D slice of the sample; (c) zoomed-in view of the subsample; (d) root phase; (e) solid phase; and (f) air phase of the subsample

diameter (ED_R), specific surface area (i.e. root surface area/root volume, *SSA*) and specific root length (i.e. length/root volume, *SRL*). Meanwhile, soil pore structure can be determined by means of PNM. Based on the modelling results, properties of pore structures including equivalent pore radius (*PER*), equivalent throat radius (*TER*), pore coordination number (*PCN*) and throat channel length (*TCL*) can be obtained. Pore tortuosity (τ), which is a measure of the curvature of flow path (i.e. ratio of the actual length of flow path to the straight distance between the ends of the path [51]) can also be determined. Based on the PNM, the water discharge rate between the pores (Q, unit: m^3) was determined by the Hagen-Poiseuille law [50, 53] by assuming laminar water flow. Based on the Darcy's law, Q was used to obtain the hydraulic conductivity (k_s, unit: m/s), which was converted to the absolute permeability (K, unit: m^2), considering water viscosity of 0.001 Pa-s.

4.2 Measurements of segmentation uncertainty

Based on different α used in the PS, different values (v) of outputs (i) of the CT-IBA, in terms of volumetric fractions and the pore and root properties (denoted as $v_{i,\alpha}$), can be determined. Accordingly, a term, called relative value (*RE;* [50]), can be used to quantify SU:

$$RE_{i,\alpha} = \frac{v_{i,\alpha} - v_{i,50\%}}{v_{i,50\%}} \qquad (8)$$

Accordingly, the value of *RE* of any output (i) can be related to α (Fig. 11(h)). In case of SU-free, *RE* is zero at any α. *RE* can thus be used to measure the uncertainty associated with phase segmentation (when using the PS method) involved in each step of CT-IBA.

SU could propagate from each step of CT-IBA to next (i.e. from the volumetric fraction to pore or root properties and eventually the hydraulic properties; Fig. 11(i)). To quantify the SU propagation from one step to the other, a SU magnification factor (SU-MF) is defined:

$$SU\text{-}MF_{i\text{-}r,\alpha} = \frac{|RE_{i,\alpha}|}{|RE_{r,\alpha}|} \qquad (9)$$

where $RE_{i,\alpha}$ is the *RE* of an output (i) of CT-IBA at a specific α; $RE_{r,\alpha}$ is the *RE* of an output r along the same SU propagation path of the output i. SU-MF = 1 means the same SU between the two steps of CT-IBA. SU-MF higher than 1 means a magnification of SU from one step of CT-IBA to the next.

4.3 Impact of SU on hydraulic properties

A series of experiments was designed to highlight the importance of conducting reliable phase segmentation of CT images for a more correct interpretation of the hydraulic properties of multi-phase rooted soil samples.

4.3.1 Test materials and methods

Clean coarse granular material and plant species with relatively coarse roots were selected for testing. The use of relatively 'simple' test materials aims to ensure that all the soil particles and most of the roots can be visualised by X-ray CT, and importantly, to control the sources of uncertainty during the process of phase segmentation. Accordingly, spherical glass beads (GB) with particle diameters ranged between 0.4 and 0.6 mm were used (d_{50}, = 0.5 mm). A cylindrical soil specimen (23 mm diameter and 48 mm height) with a uniform dry density of 1.48 g/cm^3 was prepared by the air pluviation technique [54]. A crop species was tested, namely Maize (*Zea mays*, Maz). The seeds were germinated with a wet germination paper in a dark environment covered with a foil film for five days at a room temperature of 23 ± 2.0 ºC (mean ± standard deviation), and relative humidity of 75% ± 3.5% in a grow tent. The germinated seeds were transplanted to the soil for further growing. To support the plant growth, the soil sample was sprayed with

distilled water daily and covered with plastic wrap on the top, maintaining the gravimetric water content of 20 ± 2%. After growing for 14 days, the top 15 mm of the glass beads, together with all the aboveground biomass developed, was trimmed. The sample was oven-dried at 45 ± 5 °C until the mass became constant and was then taken for X-ray CT scan. The soil samples were then scanned using the X-ray scanner at the HKUST. The voltage, current and resolution of the scanner were set to be 140 kV, 200 μA and 23.4 μm, respectively.

4.3.2 Analysis results

Figure 12(a) shows the 3-D CT image of the sample and the position of a selected subsample (554 × 554 × 554 pixel[3] (Fig. 12(b)) used for further analysis (Fig. 12(c)). Figures 12(d) to (f) are the results of segmentation of the root, bead and air (or pore) using the PS method at α = 50%. Figure 13 shows the effects of SU on volumetric content of roots (θ_R) and root phenotype. Increasing α reduced θ_R, especially when α increased from 10% to 50% (Figs. 13(a) to (c)). Simultaneously, the root surface became smoother as more uncertain curved volumes on the root surface were eliminated. Two roots, Root1 and Root2, were identified for morphological analysis. Figure 13(f) shows the skeleton of Root1 and Root2. The RE-α plots of three root phenotypic parameters, namely SSA, SRL and ED_R, are depicted in Figs. 13(g) to (i). The trends of these three parameters between Root1 and Root2 were similar. The RE of SSA reduced from 10% to 50% exponentially, whereas that of SRL increased almost linearly. Meanwhile, the RE of ED_R reduced relatively slightly with increasing α. These results suggest that ED_R are relatively more sensitivity to the SU of the root phase of the image.
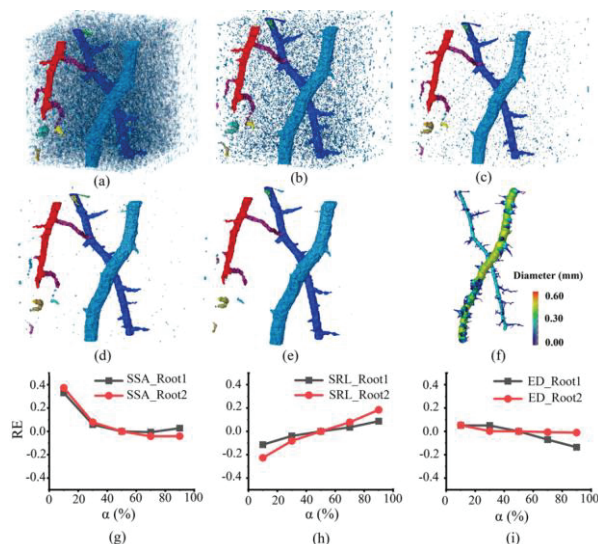

Fig. 13 Effects of SU on θ_R and root phenotype: (a) to (e) root phase when α was increased from 10%, 30%, 50%, 70% and 90%; (f) Skeletons of Root1 and Root2; and the RE-α plots for (g) SSA; (h) SRL; and (i) ED_R.

Figure 14(a) shows the results of PNM at α = 50%. Figures 14(b) to (d) are RE-α plots of the pore structure parameters of the sample. Evidently, the parameters of

pore structures (PCN and PER) are more sensitive to SU than those of throat (TER and TCL). Meanwhile, τ displayed a marginal change with α and is much less suspectable to SU.
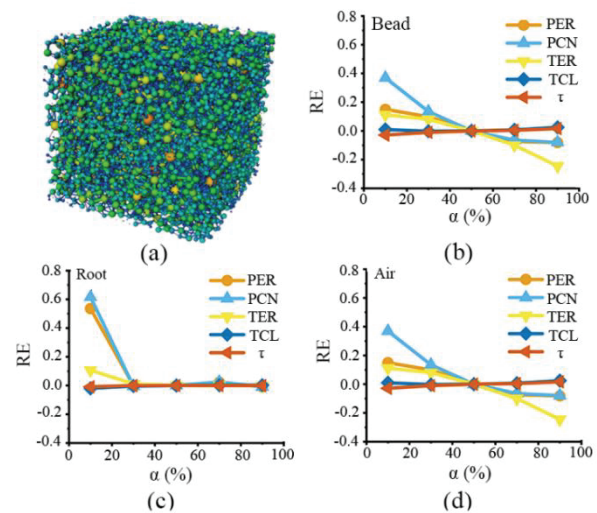

Fig. 14 (a) The model after PNM; and the RE-α plots for various pore structural parameters when varying the α of the (b) bead phase, (c) root phase; and (d) air phase.

Figure 15 shows the propagation of SU. The analysis results showed that in general, SU-MFs increased from one step of CT-IBA (i.e. the volumetric fraction) to the next (i.e. pore structure or root phenotypic parameters and k_s). Evidently, the SU-MFs using θ_B as the reference for the subsequent CT-IBA (Fig. 15(a)) were the largest when compared to using the volumetric fractions of the other two phases. The magnification of SU in this case can be up to 6 when using θ_B to estimate the pore structural parameters. The magnification can increase to even more than 10 when used for k_s estimation. Interestingly, the SU-MFs based on θ_R were always less than 1.0 (Fig. 15(b)), meaning that there was no propagation of SU. Indeed, determining θ_R has a greater SU compared with other phases. However, the value of θ_R in the sample was much smaller than θ_B and θ_A; this explains why θ_R introduced only minimal influence on the SU propagation. When using θ_A as the basis, the SU-MFs were slightly more than 1 but were not as high as those when using θ_B (Fig. 15(c)). It is interesting to observe that the SU of TCL and τ was not magnified, implying that these two properties were less affected by the process of phase segmentation.

5 Pore-level root-soil interaction

The development of the new machine learning-based X-ray CT image interpretation now permits detailed study of the root–soil physical interaction at pore-level, which is fundamental to revealing the underlying mechanisms of root-induced changes in soil hydraulic properties. In this section, a series of experiments was carried out to measure and explain how plant roots alter the soil pore structure and affect the soil water retention ability.
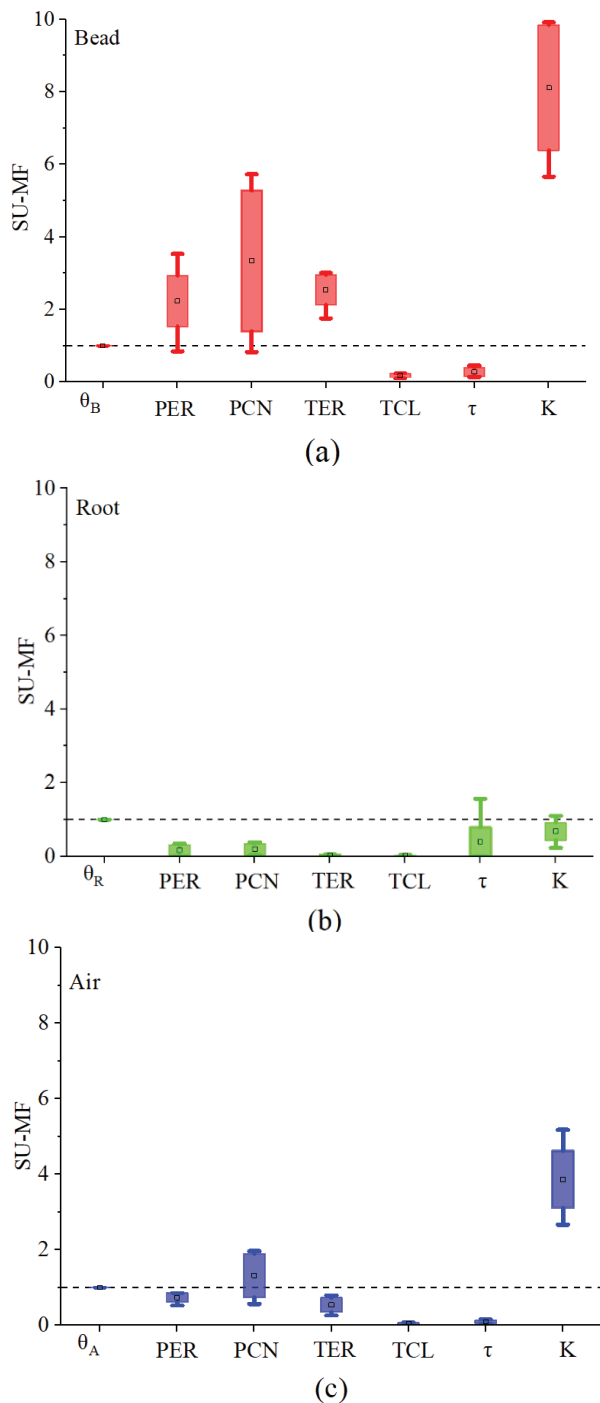
Fig. 15 SU propagation when (a) θ_B; (b) θ_R; and (c) θ_A are used as the basis of calculating SU-MF for the pore structural parameters

5.1 Test materials and methods

The same type of GB used in section 4 was selected for testing, for the same purpose of visualising all individual particles by X-ray CT. A cubic sample (50 mm length each side) with a dry density of 1.48 g/cm³ (medium dense) was prepared by the air pluviation technique. A crop species, namely barley (*Hordeum vulgare*, Bar), was tested. Three GB samples were prepared, one without plant (control) and two with plants. One of the planted samples had one seed (denoted as Bar1), whilst the other one had four seeds (denoted as Bar4). Both the planted samples were grown for two months. The

method of seed germination was identical to that adopted in section 4. During a growth period of two months, the plants were irrigated with a half-strength Hoagland solution to support plant growth [55]. Prior to testing, the above-ground biomass of the plants was removed and then the samples were taken for X-ray CT scanning using the same settings stated in section 4. Phase segmentation of the CT images was performed using the machine learning-based method introduced in section 4.1. The voltage, current and resolution of the scanner were set to be 130 kV, 200 µA and 30.2 µm, respectively. After scanning, all three samples were submerged in deaired water for three days, reaching an initial S_r of always higher than 98.0%.

Figure 16 shows the test setup used to measure the WRC of the three samples through evaporation. Each sample was instrumented with two tensiometers (10 and 40 mm from the sample surface), of which the ceramic disk has an AEV of 100 kPa, and was hung on a stable frame via a high-resolution (up to 0.01 g) load cell to measure any change in the sample weight during testing. The surface of the initially saturated samples was dried by natural evaporation in the laboratory (temperature: 30 ± 1.5 °C and relative humidity: 35 ± 2.5 %), whereas the bottom boundary of these samples was impermeable. During evaporation, the increase in matric suction and the reduction in water content was measured by two tensiometers and a load cell, respectively. The main drying WRC of the samples were obtained by relating the average suction measured by the two tensiometers with VWC (assuming no volume change of the GB during evaporation). After testing, all individual root systems were carefully exhumed from the two planted samples for detailed inspection.
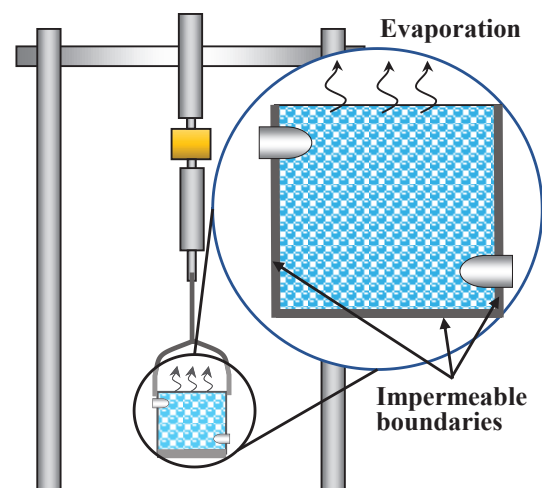

Fig. 16. Schematic test setup for measuring WRC and HCF

5.2 Results and discussion

5.2.1 Root traits

Figure 17 shows the images of the root systems collected from the planted sample Bar4. The Maize has a taproot system; several relatively coarse roots were grown from each seed and there were secondary roots of smaller diameter stemmed from the taproots. It can be seen that

Fig. 17. Images of the four individual root systems exhumed from the planted sample Bar4 after testing.

there was substantial amount of the particles of GB adsorbed on the surface of almost all the roots. It has been well known that roots would secrete a viscous fluid called exudates to the rhizosphere (i.e. a narrow region in the vicinity of roots where soil microbial activities are high; [56]) to facilitate root growth and water uptake at the root–soil interface [57]. These viscous exudates have certain cohesion which formed physical bonding with the GB particles in the vicinity of the roots. The exudates made the rhizosphere soil to have a rather different water retention properties from bulk soil [58]. Recent neutron radiography images of capturing *in-situ* process of root-water uptake [59] have showed that the rhizosphere soil typically exhibited delayed wet–dry responses when compared with the bulk soil, a strategy that plants use to maintain water supply and prevent extreme drought.

The frequency diagrams of equivalent root diameter of the two planted samples, as obtained by the CT-IBA, are shown in Fig. 18. In general, the predominant range of root diameter fell between 0.1 to 0.5 mm, consistently for both the samples. Comparatively speaking, Bar4 had less smaller roots than Bar1, probably because the four individual plants grown in the former sample exhibited more intense competition for the resources available in the growth medium. Effects of resource competition on root growth pattern and root morphology have similarly been observed from previous tests when plants were grown in close spacing [23].
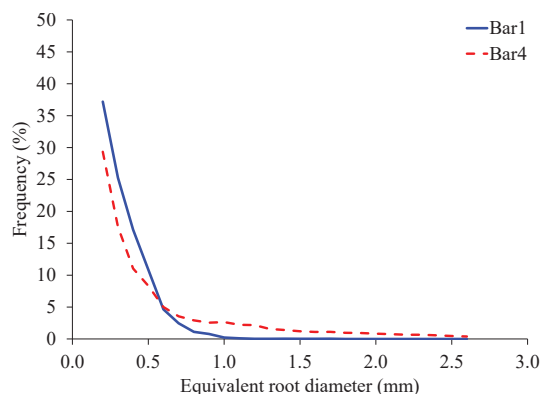

Fig. 18. Comparison of the frequency diagrams of the equivalent root diameter between the two planted samples

Figure 19 shows the vertical distributions of the root volume ratio (R_v; i.e. ratio of the root volume to the soil volume for a depth interval) of the two planted samples, obtained from CT-IBA. As expected, more root biomass was found in the top 10 mm, where the seed(s) was/were placed and where the roots started growing. Certainly, R_v was much higher for the case of Bar4 when four seeds were grown. It is worth noting that this planted sample has more root volume developed at much deeper depths than Bar1, though the values of R_v found were not as high as those identified in the shallower depths.
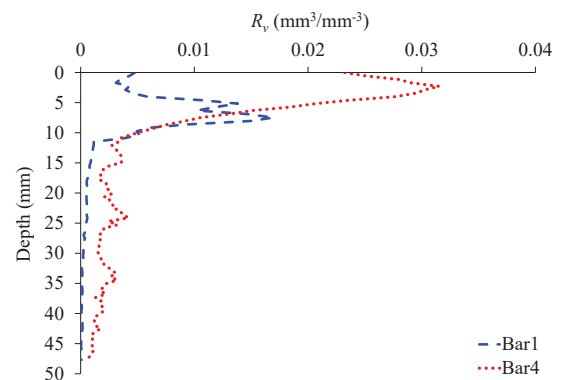

Fig. 19. Comparison of the vertical profiles of root volume ratio (R_v) between the two planted samples

5.2.2 Water retention curves

Figure 20 shows the drying WRC of the bare and two planted samples. Note that the WRC was expressed in terms of VWC, instead of degree of saturation, to highlight how the presence of plant roots may affect the porosity (i.e. the value of saturated VWC at zero suction. The initial degree of saturation before the start of the evaporation test was more than 98%. The test results shown in the figure reveal that the bare case has an AEV of approximately 1 kPa, beyond which the VWC reduced substantially until a residual suction of 2.5 kPa was reached. The planted sample that had one seed (i.e. Bar1) displayed similar values of porosity and AEV. Though this planted sample showed a slightly faster desorption rate and a smaller residual suction of 2 kPa.

When four seeds were grown in the planted sample Bar4, a much more evident change in the WRC is observed; there was a substantial increase in the porosity and reduction in both the AEV from 1 kPa (bare case) to 0.5 kPa and the residual suction from 2.5 kPa (bare case) to 1 kPa. Meanwhile, the desorption rate was similar to the case of the sample Bar1.
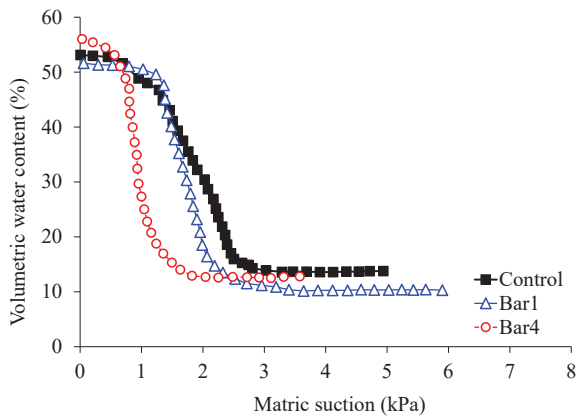

Fig. 20. Measured drying WRCs of the bare sample (control) and two planted samples (Bar1 and Bar4)

5.2.3 Soil pore evolution upon root permeation

Figures 21(a) to (c) show the spatial distribution of the local porosity of GB at a midplane of a cubic subsample (23.89 mm side) of the three samples, based on the analysis of CT images obtained right before the start of the evaporation test. Whilst the porosity field of the control case was rather uniform (Fig. 21(a)), the porosity fields around the roots in the two planted samples had been severely distorted (Figs. 21(b) and (c)). The local distortion of the porosity fields upon root penetration during growth was responsible for the overall porosity change in the planted samples (Fig. 21(d)). Compared to the control case (bare), the presence of roots introduced remarkable increases in the porosity of the entire growth medium, making the overall packing looser. Relatively speaking, the 'loosening' effect in the planted sample Bar1 was prominent mainly in the top 20 mm, where the majority of the roots were found (Fig. 19). In contrast, the 'loosening' effect was more substantial for the planted sample Bar4, in which case the porosity of the entire depth increased remarkably (Fig. 21(d)).
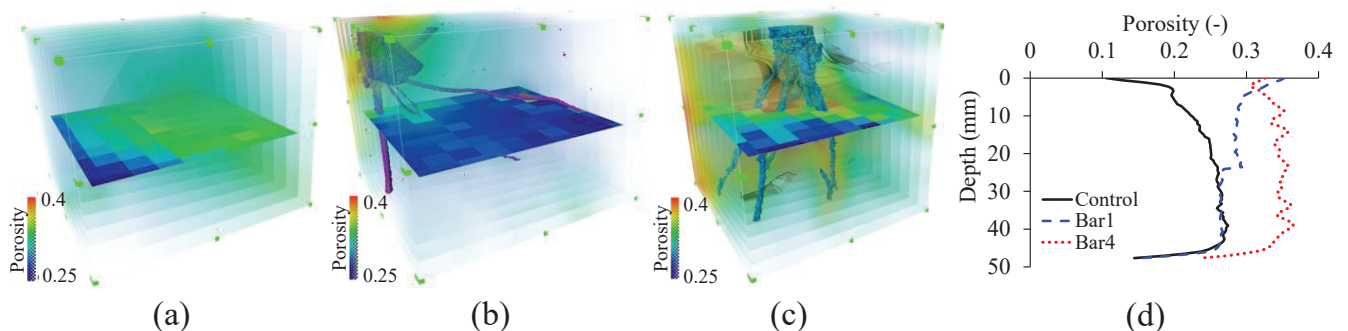

(a)

(b)

Fig. 22. Frequency diagrams of (a) equivalent pore diameter; and (b) orientation of equivalent pore throat of the control sample and the two planted samples

The frequency diagrams of the equivalent pore diameter obtained from the PNM of the three samples are compared in Fig. 22(a). Indeed, the presence of roots (with diameters ranged from 0.1 to 0.5 mm; Fig. 18) increased the pore size of the GB; the peak pore diameter was increased from 0.5 (control case) to about 0.6 mm (the two planted cases). The modification of the pore size was attributed to (1) the particle rearrangement as the roots sought for space to thicken and penetrate upon growth; and (2) the increase in organic content in the rhizosphere soil as roots released and deposited exudates (Fig. 17). These potential mechanisms undertaken by roots to modify the pore size are consistent with the observed increase in the porosity given in Fig. 21(d). Though the root penetration process in both planted samples simultaneously created some smaller pores with

(a) (b) (c) (d)

Fig. 21. Spatial distribution of porosity of GB at the midplane of a cubic subsample (23.89 mm side) of the (a) control sample; and the planted samples (b) Bar1; (c) Bar4; and the vertical profile of overall porosity of the three samples
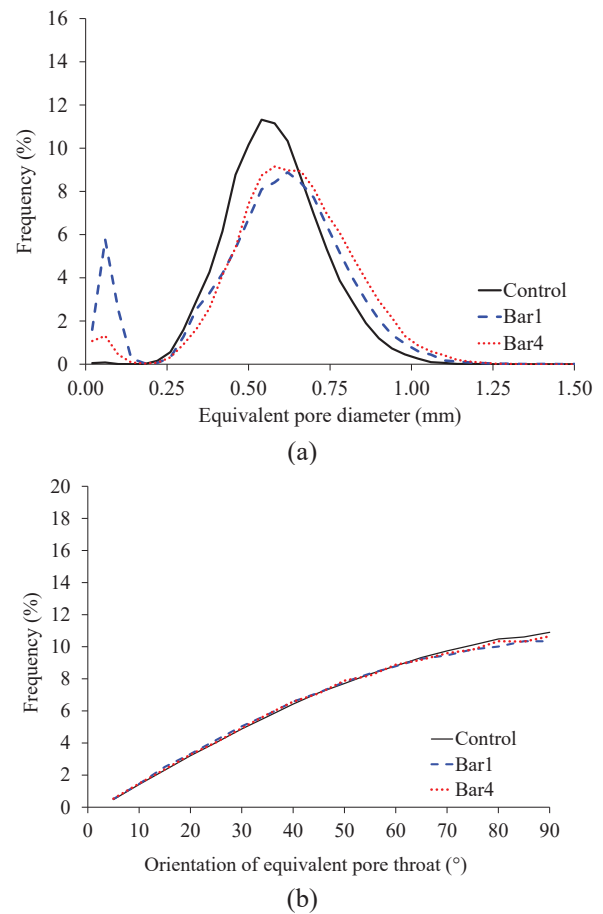
diameters less than 0.2 mm, possibly attributable to the bead rearrangement and the associated changes in pore structure. Interestingly, the root penetration process did not introduce practical change in the pore orientation (Fig. 22(b)). The 'loosening' effects introduced by the plant roots (i.e. root-induced increase in the porosity of GB) explained (1) the higher value of saturated VWC found in the planted sample Bar, when compared with the control case (Fig. 20); and (2) the observed reduction in the water retention capability for the planted samples, as the AEV and the desorption rate became smaller and greater, respectively.

The mechanisms undertaken by the roots of barley to alter the pore structure of GB depicted in Figs 20 to 22 were rather different from what was hypothesised by [20] through a conceptual capillary model and by [22, 23] based on the laboratory findings (e.g. Fig. 3) of silty sand permeated by woody roots of a shrub species. Although the roots of barley did occupy some pore space of GB like what has been considered in existing WRC model [Eqs (1) to (3); 23], the 'loosening' effects caused by the root penetration process were not captured. Indeed, the model implicitly assumes that the soil skeleton remains rigid as roots penetrate and occupy the pore space. It may also be worth mentioning that, at least for the GB-barley system examined in this section, capturing the root-induced change in pore size may be adequate to model the WRC of rooted soils, as the root-induced change in pore orientation may be neglected.

6 Concluding remarks and outlook

It has been evident that permeation of plant roots in soil matrix upon growth and penetration could remarkably influence the hydraulic properties of unsaturated soils, including WRC and HCF. There properties are vitally important to conducting seepage and stability analyses of bioengineered slopes. The developments of advanced X-ray testing apparatus and AI-enabled image analysis techniques in this study have made the visualisation and quantification of detailed pore-level physical interaction of two natural materials, namely unsaturated soils and plants, under different controlled stress states possible. AI has enabled the phase segmentation process of CT images of multi-phase unsaturated rooted soils, which are often challenging due to the close coefficients of X-ray attenuation of some of the phases (e.g., water and (moist) roots) more accurate and reliable. The combined use of these new technologies can now quantify *in-situ* spatiotemporal evolution of soil pore structure (e.g., size, orientation and connectivity) due to external stress or/and root penetration and thickening in the soil matrix. Evaluation of the performance of the AI-enabled phase segmentation algorithm suggests that although the root phase has the largest uncertainty among other phases, its volumetric fraction is relatively low and thus it does not contribute much to the error propagation of estimating the pore structure in the subsequent image analysis.

The uses of these technologies have led to new discoveries to aid the understanding of the mechanics of unsaturated soils and their physical interaction with plant roots: (1) the observed increases in water retention capability of bare soil (i.e. medium dense Toyoura sand, in this study) following the increases in net normal stress were due to the decrease in pore size and its distribution, whereas any stress-induced changes in pore orientation and pore connectivity were practically negligible; and (2) root growth of a crop species, barley, in the median dense, poorly-graded glass bead caused an increase in the porosity upon bead arrangement due to the processes of root penetration and thickening, eventually leading to a reduction in water retention capability (i.e. decrease in AEV and increase in desorption rate). The latter findings do not accord with what was hypothesised previously in the literature when pore-level root–soil interaction was unavailable; root occupation of the pore space of growth medium along, without capturing local porosity changes due to particle rearrangement upon root penetration and thickening as discovered in this study, is inadequate to fully explain the root-induced changes in the hydraulic properties of the growth medium. Nonetheless, the root–soil interaction mechanisms revealed in this study were based on a rather simple soil–plant system, where each individual particles and roots can be visualised to aid the evaluation of the performance of the newly proposed AI-enabled phase segmentation algorithm. Whether the same root–soil physical interaction discovered (e.g., soil 'loosening' upon root penetration and thickening) in a more realistic system deserves further investigation.

Pore-level study of root–soil physical interaction via non-invasive means such as CT imaging and others has been a common approach to learn the root phenotype of crop species to aid crop management plan for addressing food security problems [e.g., 60]. In the applications of geotechnical engineering where soil behaviours altered by plant roots are of major concern, research of this kind of pore-level root–soil interaction is at its infancy stage. Only in recent years has micromechanical root–soil interaction been studied in terms of how root exploration in the soil pore space affects the kinematics of soil grains [31] and how the kinematics of roots evolve as their mechanical properties are mobilised to resist external loading transferred from the soil [61]. Certainly, more research is needed to reveal the underlying mechanisms, especially at pore-scale which (1) underpins many root–soil physical interaction that cannot be easily identified at element scale or larger; and (2) are fundamentals to unify the root effects on the hydromechanical properties of unsaturated soils, aiding the explanation of some of the contradicting data found in the literature. It should not be forgotten that the exudates released by plant roots and deposited in the soil a few millimetres nearby (i.e. rhizosphere soil), hence the biochemical modification of the soil in this zone, could substantially affect the soil–root interface behaviour such as water uptake efficiency [59] and potentially interface shearing properties that control the root failure mode (breakage vs pull-out [4]). Characterising the role of vegetation on the changes in hydromechanical properties of unsaturated soils under varying saturation conditions, on the basis of pore-level micro-hydromechanics, is a key to further advance and develop more scientifically-sound constitutive stress–strain and flow relationships of unsaturated rooted soils, which govern the analysis and design of the engineering behaviour of bioengineered soil slopes.

References

1. Stokes, G. B. Douglas, T. Fourcaud, F. Giadrossich, C. Gillies, T. Hubble, J. H. Kim, K. W. Loades, Z. Mao, I. R. McIvor, S. B. Mickovski, S. Mitchell, N. Osman, C. Phillips, J. Poesen, D. Polster, F. Preti, P. Raymond, F. Rey, M. Schwarz, L. R. Walker, Plant Soil **377**, 1 (2014)

2. D. Boldrin, A. K. Leung, A. G. Bengough, Géotechnique **71**, 970 (2021)

3. A. A. Karimzadeh, A. K. Leung, S. Hosseinpour, Z. Wu, P. Fardad Amini, Can. Geotech. J. **58**, 1915 (2021)

4. J. Zhu, A. K. Leung, Y. Wang, Plant Soil **480**, 675 (2022)

5. G. J. Meijer, D. Muir Wood, J. A. Knappett, A. G. Bengough, T. Liang, Géotechnique (2022) (In press)

6. B. M. Świtała, A. Askarinejad, W. Wu, S. M. Springman, Géotechnique **68**, 375 (2018)

7. A. A. Karimzadeh, A. K. Leung, Z. Gao, Géotechnique (2022) (In press)

8. A. A. Karimzadeh, A. Kwan Leung, P. F. Amini, J. Geotech. Geoenvironmental Eng. **148**, 06021016 (2022)

9. A. Fraccica, E. Romero, T. Fourcaud, Geomech. Energy Environ. **30**, 100303 (2022)

10. G. J. Meijer, D. Muir Wood, J. A. Knappett, G. A. Bengough, T. Liang, Int. J. Numer. Anal. Methods Geomech. **43**, 684 (2019)

11. B. M. Świtała, W. Wu, Géotechnique **68**, 481 (2018)

12. K. Mahannopkul, A. Jotisankasa, Soils Found. **59**, 500 (2019)

13. D. Boldrin, A. K. Leung, A. G. Bengough, Plant Soil **416**, 437 (2017)

14. A. Yildiz, F. Graf, C. Rickli, S. M. Springman, Proc. Inst. Civ. Eng. - Geotech. Eng. **172**, 507 (2019)

15. H. Rahardjo, A. Satyanaga, E. C. Leong, V. A. Santoso, Y. S. Ng, Soils Found. **54**, 417 (2014)

16. A. K. Leung, V. Kamchoom, C. W. W. Ng, Can. Geotech. J. **54**, 291 (2017)

17. C. W. W. Ng, V. Kamchoom, A. K. Leung, Landslides **13**, 925 (2016)

18. T. L. Zhan, C. W. Ng, D. G. Fredlund, Can. Geotech. J. **44**, 392 (2007)

19. C. W. W. Ng, J. J. Ni, A. K. Leung, Géotechnique **70**, 867 (2020)

20. C. Scanlan, C. Hinz, *Insights into the processes and effects of root-induced changes to soil hydraulic properties*, in Proceedings of the 19th World Congress of Soil Science, WCSS, 1-6 August 2010, Brisbane, Australia (2010)

21. A. Jotisankasa, T. Sirirattanachat, Can. Geotech. J. **54**, 1612 (2017)

22. C. W. W. Ng, J. J. Ni, A. K. Leung, Z. J. Wang, Géotechnique Lett. **6**, 106 (2016)

23. J. J. Ni, A. K. Leung, C. W. W. Ng, Can. Geotech. J. **56**, 1049 (2019)

24. D. Boldrin, A. K. Leung, A. G. Bengough, Plant Soil **431**, 347 (2018)

25. D. Gallipoli, S. J. Wheeler, M. Karstunen, Géotechnique **53**, 105 (2003)

26. L. Song, J. H. Li, T. Zhou, D. G. Fredlund, Ecol. Eng. **103**, 207 (2017)

27. J. Ni, A. K. Leung, C. W. W. Ng, Géotechnique **69**, 554 (2019)

28. K. K. Watson, Water Resour. Res. **2**, 709 (1966)

29. A. K. Leung, J. L. Coo, C. W. W. Ng, R. Chen, Can. Geotech. J. **53**, 1332 (2016)

30. M. Th. van Genuchten, Soil Sci. Soc. Am. J. **44**, 892 (1980)

31. D. J. Bull, J. A. Smethurst, I. Sinclair, F. Pierron, T. Roose, W. Powrie, and A. G. Bengough, Proc. R. Soc. Math. Phys. Eng. Sci. **476**, 20190838 (2020)

32. Y. Higo, F. Oka, S. Kimoto, T. Sanagawa, Y. Matsushima, Soils Found. **51**, 95 (2011)

33. J.-P. Wang, E. Andò, P. Charrier, S. Salager, P. Lambert, B. François, Géotechnique Lett. **9**, 269 (2019)

34. J. Liu, A. K. Leung, C. Zhou, R. Chen, Can. Geotech. J. (2022) (In press)

35. Otsu, N. IEEE Transaction on Systems, Man and Cybernetics, **9**(1): 62–66. (1979)

36. Sochi, T. PhD thesis, Imperial College London, U. K. (2010).

37. C. W. W. Ng, Y. W. Pang, J. Geotech. Geoenviron., ASCE, **126**, 157-166 (2000).

38. C. W. W. Ng, A. K. Leung, J. Geotech. Geoenviron., ASCE, **138**, 58-68 (2012).

39. S. R. Tracy, C. R. Black, J. A. Roberts, C. Sturrock, S. Mairhofer, J. Craigon, S. J. Mooney, Ann. Bot. **110**, 511 (2012)

40. M. Soret, S. L. Bacharach, I. Buvat, J. Nucl. Med. **48**, 932 (2007)

41. C. Douarre, R. Schielein, C. Frindel, S. Gerth, D. Rousseau, J. Imaging **4**, 65 (2018)

42. A. G. Smith, J. Petersen, R. Selvan, C. R. Rasmussen, Plant Methods **16**, 13 (2020)

43. Z. Xu, C. Valdes, and J. Clarke, Agronomy **8**, 71 (2018)

44. M. P. Pound, J. A. Atkinson, A. J. Townsend, M. H. Wilson, M. Griffiths, A. S. Jackson, A. Bulat, G. Tzimiropoulos, D. M. Wells, E. H. Murchie, T. P. Pridmore, A. P. French, GigaScience **6**, gix083 (2017)

45. P. C. Baveye, M. Laba, W. Otten, L. Bouckaert, P. Dello Sterpaio, R. R. Goswami, D. Grinev, A. Houston, Y. Hu, J. Liu, S. Mooney, R. Pajor, S. Sleutel, A. Tarquis, W. Wang, Q. Wei, M. Sezgin, Geoderma **157**, 51 (2010)

46. M. Phalempin, E. Lippold, D. Vetterlein, S. Schlüter, Plant Methods **17**, 39 (2021)

47. S. Schlüter, A. Sheppard, K. Brown, D. Wildenschild, Water Resour. Res. **50**, 3615 (2014)

48. P. Agrawal, A. Mascini, T. Bultreys, H. Aslannejad, M. Wolthers, V. Cnudde, I. B. Butler, A. Raoof, Adv. Water Resour. **155**, 103991 (2021)

49. V. A. J. Jaques, A. D. Plessis, M. Zemek, J. Šalplachta, Z. Stubianová, T. Zikmund, J. Kaiser,

Meas. Sci. Technol. **32**, 122001 (2021)

50. M. C. Krygier, T. LaBonte, C. Martinez, C. Norris, K. Sharma, L. N. Collins, P. P. Mukherjee, S. A. Roberts, Nat. Commun. **12**, 5414 (2021)

51. T. R. Ferreira, N. L. Archilha, L. F. Pires, J. Hydrol. **612**, 128024 (2022)

52. C. F. Berg, Transp. Porous Media **103**, 381 (2014)

53. R. Song, Y. Wang, J. Liu, M. Cui, and Y. Lei, Energy Sci. Eng. **7**, 2842 (2019)

54. S. Miura, S. Toki, Soils Found. **22**, 61 (1982)

55. D. R. Hoagland, and D. I. Arnon, California agricultural experiment station, **347**. (1950)

56. M. Nazari, S. Bickel, P. Benard, K. Mason-Jones, A. Carminati, & M. A. Dippold, Front. Plant Sci. **12**, 3285 (2022)

57. P. Benard, M. Zarebanadkouki, M. Brax, R. Kaltenbach, I. Jerjen, F. Marone, A. Carminati, Vadose Zone J. **18**, 1-10 (2019)

58. M. Naveed, M. A. Ahmed, P. Benard, L. K. Brown, T. S. George, A. G. Bengough & P. D. Hallett, Plant Soil, **437**, 65-81 (2019).

59. M. Zarebanadkouki, & A. Carminati, J. Plant Nutr. Soil Sci., **177**, 227-236 (2014)

60. S. R. Tracy, K. R. Daly, C. J. Sturrock, N. M. Crout, S. J. Mooney, and T. Roose, Water Res. Research, **51**(2), 1006-1022 (2015)

61. F. Anselmucci, E. Andó, G. Viggiani, N. Lenoir, R. Peyroux, C. Arson, and L. Sibille. Geotechnique Letts., **11**(1), 96 – 102 (2021)